Computational Study of Rotating-Stall Inception in Axial Compressors

L. He*

University of Durham, Durham DH1 3LE, England, United Kingdom

Rotating-stall inception in axial-flow compressors has been studied computationally using a quasi-three-dimensional time-marching Navier–Stokes method with a mixing-length turbulence model. Of particular interest was the effect of external circumferential disturbances corresponding to inlet stagnation pressure distortions and rotor/stator blade interactions. The present results show that rotating stall onset patterns in terms of number of stall cells and rotating speeds were influenced by small external circumferential stationary or rotational disturbances. First mode circumferential disturbances had the most destabilizing effect, resulting in a single-cell pattern rotating in the absolute frame at about 50% rotor speed, as is observed in most experiments. Short-scale multiple-cell patterns rotating at a higher absolute speed could also be excited by a disturbance with the same circumferential length scale. Short-scale multiple-cell patterns tended to be more persistent in an isolated blade row than in a stage. In the latter case, a short-scale pattern initiated by a rotor–stator interaction would quickly change into a long-scale single-cell pattern, associated with a distinct change of the rotating speed.

Nomenclature

Amp_0 = nondimensional amplitude of inlet stagnation pressure perturbation
C = blade chord length
ds = differential length element with unit outward-pointing normal vector
e = internal energy
F = flow fluxes across unit area in x direction
h = streamtube height
NB_r = number of rotor blades
NB_s = number of stator blades
$\boldsymbol{n}_x$ = unit vector in x direction
P_0 = inlet stagnation pressure
P_{0R} = relative inlet stagnation pressure
P_2 = exit static pressure
p = static pressure
r = radius
T = temperature
t = time
U = primitive flow variable
U_R = rotation speed of rotor blades
u = flow velocity in x direction
u_g = mesh grid velocity in x direction
v = flow velocity in y direction
x = axial coordinate
y = circumferential coordinate
μ = viscosity coefficient
ρ = flow density

Subscript
i = circumferential mesh point index

I. Introduction

THE development of computer hardware and numerical methods has resulted in the wide application of computational fluid dynamics (CFD) to the field of turbomachinery aerodynamics. Although the accuracy of a numerical calculation is still subject to turbulence modeling, meshing, and the basic numerical scheme adopted (which are areas of current and future research), the usefulness of CFD calculations in compressor/turbine design has been well demonstrated. It is probably equally important to recognize that the development of CFD methods has resulted in very useful analysis tools that are able to provide detailed information to enhance the understanding of complex flow physics at design and off-design conditions. The objective of the present computational study was to examine the onset of rotating stall in compressor/fan blade rows.

Rotating stall is seen as a transient intermediate stage between normal flow and complete flow breakdown leading to engine surge. Because of the complex and transient nature, it is difficult to either understand or model the onset of rotating stall. Previous work has been devoted mainly to machine design based on extrapolation of experience. In the recent years there has been revived interest in the research of rotating-stall inception, driven mainly by the new development of active suppression of flow instabilities (rotating stall and surge) in compressor systems (e.g., the work by Epstein et al.[1] and Day[2]). To implement effectively techniques for active control of rotating stall, our current understanding and modeling of the inception mechanism needs to be improved.

Most conventional methods for modeling rotating stall follow the lumped-parameter approach.[3,4] The basic assumption is that the length scales of disturbances are much larger than one blade pitch, so that a given blade row characteristic may be used locally in both a spatial and temporal sense. This approach predicts the existence of long-scale modal waves leading to rotating stall. The prestall modal waves have been observed in some experiments, however, it has been found in other experiments (e.g., those by Day,[5] that a short-scale spike disturbance can also be responsible for rotating-stall inception). It has been suggested[6] that the short-scale spike behavior initiating rotating stall might have to be explained in a three-dimensional context.

Notable progress in the use of CFD-type techniques for the calculation of rotating stall has been made by Sisto et al.[7] and Jonnavithula et al.[8] The basic flow model adopted is a two-dimensional discrete vortex model with the separation point being obtained by an integral boundary-layer method. The evolution of rotating stall is well predicted when compared with their experiment,[8] although only up to six blade passages are used in the computation.

*Lecturer, School of Engineering.

In the present work, a computational study has been carried out aimed at identifying the feasibility of simulating rotating stall inception using a two-dimensional (quasi-three-dimensional) time-marching Navier–Stokes solver and improving the understanding of the stall inception mechanism. A two-dimensional calculation method was regarded as a natural first step towards building up a full three-dimensional simulation. In addition, it seems that much could still be learned by using a two-dimensional method capable of resolving short-scale disturbances. In the light of the current research interest in the long-length-scale prestall modal wave mechanism against the short-length-scale spike mechanism, it would be useful to identify if short-length-scale spikes could possibly exist in a two-dimensional context.

II.   Numerical Method

A.   Governing Equation and Discretization

For convenience in dealing with unsteady flows in multiple blade rows, an absolute cylindrical coordinate system is adopted. This simplifies the treatment of the interface between meshes attached to relatively moving blade rows and the evaluation of the extra terms resulting from rotating of the coordinate system is not needed. The integral form of the quasi-three-dimensional unsteady Navier–Stokes equations over a moving finite area ΔA is

$$\frac{\partial}{\partial t} \iint_{\Delta A} U \, dx \, dy + \oint_S [(F - Uu_g - V_x)\mathbf{n}_x$$

$$+ (G - Uv_g - V_y)\mathbf{n}_y] \cdot d\mathbf{s} = \iint_{\Delta A} S \, dx \, dy \qquad (1)$$

where

$$U = h \begin{bmatrix} \rho \\ \rho u \\ \rho vr \\ \rho e \end{bmatrix} \qquad F = h \begin{bmatrix} \rho u \\ \rho uu + p \\ \rho uvr \\ (\rho e + p)u \end{bmatrix}$$

$$G = h \begin{bmatrix} \rho v \\ \rho uv \\ (\rho vv + p)r \\ (\rho e + p)v \end{bmatrix} \qquad S = \begin{bmatrix} 0 \\ p\frac{\partial h}{\partial x} \\ 0 \\ 0 \end{bmatrix}$$

The quasi-three-dimensional effect is introduced by allowing specified variations of r and h in the axial direction. Both u_g and v_g are the moving mesh grid velocities, to accommodate the rotation of the mesh attached to rotor blades and blade vibration.[9,10] In this article only the former is considered, thus u_g is zero and v_g is equal to the blade rotation velocity. V_x and V_y are the viscous terms:

$$V_x = h \begin{bmatrix} 0 \\ \tau_{xx} \\ r\tau_{xy} \\ -q_x + u\tau_{xx} + v\tau_{xy} \end{bmatrix} \qquad V_y = h \begin{bmatrix} 0 \\ \tau_{xy} \\ r\tau_{yy} \\ -q_y + u\tau_{xy} + v\tau_{yy} \end{bmatrix}$$

where

$$\tau_{xy} = \frac{2}{3}\mu\left(2\frac{\partial u}{\partial x} - \frac{\partial v}{\partial y}\right), \qquad \tau_{yy} = \frac{2}{3}\mu\left(2\frac{\partial v}{\partial y} - \frac{\partial u}{\partial x}\right)$$

$$\tau_{xy} = \mu\left(\frac{\partial u}{\partial y} + \frac{\partial v}{\partial x}\right), \qquad q_x = -k\frac{\partial T}{\partial x}, \qquad q_y = -k\frac{\partial T}{\partial y}$$

The coefficient μ is obtained from the Sutherland's law with a reference viscosity coefficient being calculated from a fixed Reynolds number at the inlet flow condition. The coefficient of heat conductivity k is related to the viscosity coefficient through a Prandtl number.

For laminar flows, the previous set of equations together with the equation of state is readily solvable. For turbulent flows, the equations, in the widely used Reynolds-averaged form, require a turbulence model to close extra stress and heat flux terms. In the present work, the standard Baldwin–Lomax mixing length model is adopted.

The governing equations are discretized in space by the finite volume method and integrated in time by using a four-stage Runge–Kutta scheme.[11] The second- and fourth-order blended smoothing is adopted in both the streamwise and circumferential directions for numerical damping.

To relax the time-step limitation on the explicit temporal integration, a time-consistent two-grid technique[9] is employed. Spatial accuracy is controlled by the basic fine mesh, an accuracy of the temporal integration is controlled by ensuring that the size of the coarse mesh is much smaller than the shortest physical length scale of interest. Typically, an increase of time-step length by a factor of 10 could be realized with adequate temporal resolution.

B.   Computational Domain Arrangement and Boundary Condition

The computational domain is a quasi-three-dimensional stream surface consisting of multiple blade passages and multiple blade rows. As intended, the domain should cover a whole annulus, the direct repeating (periodic) condition is applied between the upper and lower boundaries.

For each blade row, an H mesh is fixed to the blades. At an interface between two adjacent rows, relatively moving meshes are patched together, with two coincident mesh lines sliding on each other (Fig. 1). At each stage of the time-marching solution, all vertex points at the interface are updated by distributing residuals from their interior adjacent cells in a one-sided manner. The numerical smoothing for these points is also treated in a one-sided manner, similar to that for points on a blade surface. Then, the information is transferred across the interface by a correction method. The correction is devised to ensure the following:

1) Any flow variable at a mesh nodal point on one side of the interface must equal that at a dummy point on the other side of the interface.

2) Any flux across a computational cell boundary on one side of the interface should equal that across a dummy boundary on the other side of the interface.
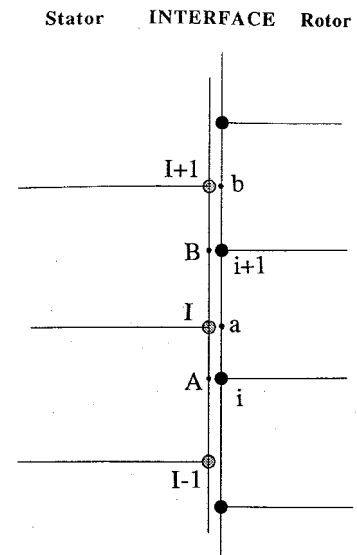

Fig. 1   Sliding interface between patched rotor and stator meshes.

Consider a general situation, as shown in Fig. 1. I and $I + 1$ are vertex mesh points of the upstream blade row with their dummy points at the boundary of the downstream row being a and b, respectively. Similarly, i and $i + 1$ are the mesh nodal points of the downstream row with their upstream dummy points being A and B, respectively. For the mesh points I (upstream row) and i (downstream row), the following simple corrections on the primitive variables are used:

Upstream row:

$$U_I^{\text{corrected}} = 0.5(U_I + U_a)^{\text{uncorrected}} \qquad (2a)$$

Downstream row:

$$U_i^{\text{corrected}} = 0.5(U_i + U_A)^{\text{uncorrected}} \qquad (2b)$$

where, for example, U_a is the variable at point a, the dummy point of I across the interface; U_A is that at point A, the dummy point of i (Fig. 1). The flow variables at the dummy points are obtained by a linear interpolation in the circumferential direction, consistent with the second-order accuracy of the spatial discretization. Numerical tests showed that the simple correction given in Eq. (2) provided an effective way of communication across the interface. Certainly, if the circumferential mesh spacings are the same on both sides of the interface and the meshes move to a position so that the mesh points on either side coincide with each other, then both requirements 1 and 2 will be satisfied.

To make the flow fluxes fully conserved across the interface for all relative positions and nonequal mesh spacings, the following corrections on the fluxes are employed:

Upstream row:

$$(F_{I,I+1}\Delta y_{I,I+1})^{\text{corrected}} = 0.5[F_{I,I+1}\Delta y_{I,I+1}$$
$$+ (F_{i,i+1}\Delta y_{a,i+1} + F_{i+1,i+2}\Delta y_{i+1,b})]^{\text{uncorrected}} \qquad (3a)$$

Downstream row:

$$(F_{i,i+1}\Delta y_{i,i+1})^{\text{corrected}} = 0.5[F_{i,i+1}\Delta y_{i,i+1}$$
$$+ (F_{I-1,I}\Delta y_{A,I} + F_{I,I+1}\Delta y_{I,B})]^{\text{uncorrected}} \qquad (3b)$$

where, for instance, $F_{i,i+1}$ is the unit flux across the cell boundary defined between y_i and y_{i+1}, and $\Delta y_{i,i+1} = \Delta y_{i+1} - y_i$.

Numerical results show that use of the flux corrections, as given by Eq. (3), ensures the conservation of the total summed fluxes across the interface to an accuracy subject only to computer machine error.

Two types of conditions are used on blade surfaces. The first is the no-slip wall condition in which the velocities are set to zero on the wall and the wall shear stress is evaluated according to the local derivatives. The second method is to set the wall shear stress from the log-law and to allow the velocities to slip. For attached boundary layers the slip-wall condition needs fewer mesh points in the near-wall region than the no-slip condition. If the flow is separated from a surface, the no-slip condition is specified.

At the inlet and outlet boundaries, ideally a nonreflecting boundary condition should be used. However, the implementation of such a condition seems to be difficult because current nonreflecting boundary condition methods are all based on a linear analysis.[12] When parameters at the boundary change in a monotonous (nonperiodic) manner, for example, a continuous outlet static pressure rise caused by throttling, it is not apparent how to define an equilibrium state on which the linear perturbations are to be based. On the other hand, nonperiodic variations of parameters at the far-field boundaries can be easily introduced in the conventional reflecting boundary conditions with specified inlet stagnation pressure, inlet stagnation temperature, inlet flow angle (or tangential velocity), and exit static pressure. By adopting long inlet and outlet far-field domains (typically with the length of the annulus corresponding to the wavelength of the first circumferential mode), spurious reflections should be minimized.

III. Results and Discussions

As far as compressor rotating stall inception is concerned, there is a certain amount of published experimental results that show the rotating-stall patterns with regard to the number of stall cells and the rotating speed during stall inception.[5,6] The first task was to identify if the present numerical method would be able to predict the features experimentally observed.

Note that stall inception in compressor experimental studies is normally detected by hot-wire probes located in an absolute system upstream of the first rotor blade row that are equally spaced around the circumference of the machine. The time-space information about formation and evolution of stall cells can be clearly seen by the axial velocities measured by these hot-wire probes. In the present computational study, four numerical axial velocity probes were circumferentially equally spaced in the stationary system at a location 25% chord upstream of the rotor blade row, as shown in Fig. 2. Since the mesh around the rotor was moved with the rotor blades, the probes would effectively be moved at the blade rotation speed in the opposite direction in the rotor relative frame. At any instant, the values of axial velocity at these probes would be obtained from adjacent mesh points by interpolation.

A. Single-Blade-Row Calculation

The present study considers a generic annulus cascade section of an isolated rotor blade row. The blades are of the double circular arc profile with a chord length of 0.035 m and relative thickness of 10%. The stagger angle is 33 deg and the chord-to-pitch ratio is 1.2. The Reynolds number based on the inlet flow parameters is 10^6 and the flow is assumed to be turbulent, starting from the leading edge. The absolute inlet flow angle is 0 deg, and the relative inlet tangential velocity (i.e., the blade rotation speed) is specified to be 90 m/s.

The blade row consists of 20 blade passages. The computational mesh is shown in Fig. 3. For this case, the blade passage region (the near field) is covered by relatively fine mesh (500×70). Reasonably far from the blade passages, disturbances with short length scales would normally decay quite quickly; only those with long length scales would be of significance. For this reason, the inlet and outlet far fields are covered by a coarse mesh ($2 \times 250 \times 25$) with its circumferential mesh spacing being twice that of the near field. The total number of mesh points is 47,500. The number of time steps to march one rotor revolution (20 blade passing periods) is 2500, for which a CPU time of 2.1 hours on an IBM 380/3AT workstation was consumed.

The inlet conditions of stagnation pressure, temperature, and the tangential velocity are fixed and the outlet static pressure is continually increased to simulate a process approaching stall along a constant rotor-speed line on the compressor performance map.
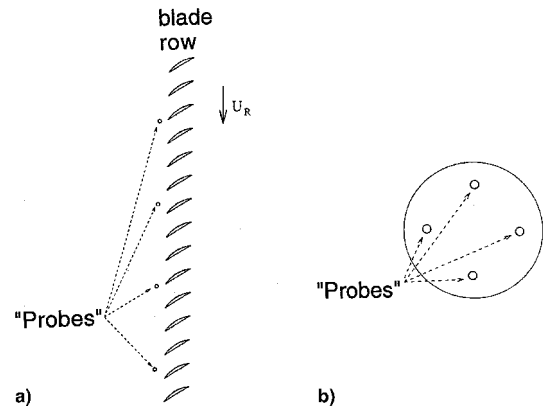

Fig. 2 Location of numerical axial velocity probes: a) cascade and b) equivalent frontal axial views.
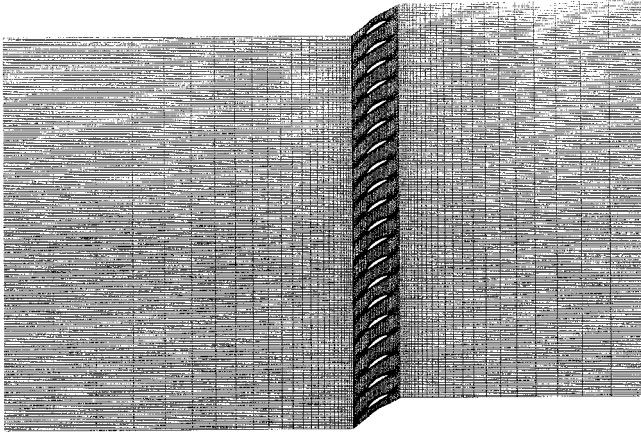
Fig. 3 Computational mesh (single rotor blade row, 20 blade passages).

A preliminary computation with a uniform inlet stagnation pressure (clean inlet) showed that a calculated rotating-stall pattern typically had multiple stall cells with a length scale covering two or three blade pitches. Time traces of axial velocity from the four upstream numerical probes with the relative outlet static pressure being increased from $P_2/P_{0R} = 0.9600$ to 0.9604 are shown in Fig. 4. For clarity, the time traces shown in Fig. 4 are shifted vertically by a constant interval. It is noticed that this calculated rotating-stall pattern seems to be very different from that commonly observed in experiments, where a single rotating-stall cell almost always comes into existence during a stall inception process.[2,5,6] From the modal-wave point of view, the single-cell pattern should be associated with the first-order modal wave with its wavelength being the circumference. In the present case, the calculated flowfield was very axisymmetrical and no indication of the first-order modal wave was observed, even when blade boundary layers became considerably separated. The reason seems to be that the background noise in the calculation was not big enough to trigger the first-order modal wave to grow. The background noise in the calculation could only derive from computer machine error, which was expected to be much smaller than typical background noise in experiments. As a result, although surface boundary layers became separated, a stable (nonrotating) flow pattern could be obtained under a higher loading condition, compared to that in a real situation. However, when the surface boundary layers on all blades over the whole annulus were fully separated, the flowfield became much more sensitive to a slight irregularity/noise, and a simple communication between a passage and its immediate neighboring passages would be able to develop into rotating-stall, resulting in a short-length-scale multiple-cell pattern such as that shown in Fig. 4.

In view of the previous observations, the effect of background disturbances would need to be considered. This was introduced by a perturbation to the inlet stagnation pressure. Here we only simulated a stationary nonuniformity (distortion) in space. The perturbation is of a sinusoidal form in the absolute frame, whereby the resultant instantaneous stagnation pressure for mesh point i at the inlet is in the form of

$$P_0 = \bar{P}_0 \left[1 + Amp_0 \sin \left(2\pi n \frac{y_i - y_1}{Y_{\text{pitch}}} \right) \right] \qquad (4)$$

where Y_{pitch} is the circumferential length of the multiple passage domain at the inlet; n is an integer that defines the spatial length scale of the perturbation, for example, $n = 1$ gives the first-mode perturbation with its wavelength being equal to the circumference; and $n = 2$ gives the second mode perturbation with its wavelength being equal to half of the circumference.

The calculations were carried out with either the first mode ($n = 1$) or the second mode ($n = 2$) perturbation, at the same amplitude, $Amp_0 = 0.003$. This perturbation in stagnation pressure corresponded to about 5% of the inlet dynamic head and was intended to be sufficiently large to overwrite the influence of the computer machine error and still small enough to be comparable to typical irregularities in a real compressor situation. The time-traces of the axial velocity from the four probes subject to the first mode inlet stagnation pressure perturbation are shown in Fig. 5, corresponding to the exit static pressure increased from 0.9570 to 0.9577. Those subject to the second mode perturbation with the exit static pressure increased from 0.9581 to 0.9589 are shown in Fig. 6. It is very clear that a single-cell rotating-stall pattern is triggered by the first mode perturbation, also shown by an instantaneous entropy contour (Fig. 7). The entropy contour is a good indication of separated vortical flow structures, because of the convective nature of entropy. Furthermore, when the flowfield is subject to the second mode P_0 perturbation, a two-cell pattern is triggered (Fig. 6). The results for these three cases are summarized in Table 1.

It can be seen that the first mode P_0 perturbation had the most destabilizing effect, the single-cell pattern being triggered at the highest flow coefficient. Using the modal wave argument, the present results might be interpreted as implying that the first-order modal wave is the most unstable, and should be seen first when all modes are equally excited.
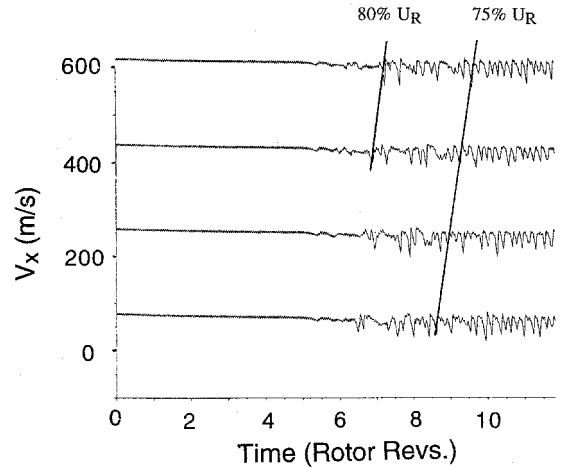

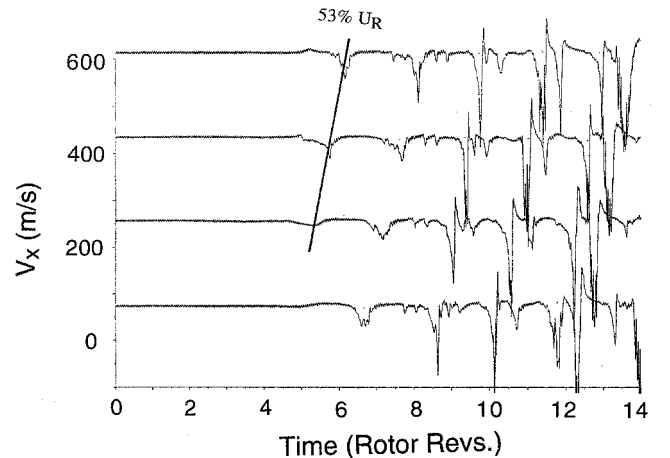**Fig. 4 Time traces of axial velocity from four upstream probes ($P_2/P_{0R} = 0.96 - 0.9604$, clean inlet).**

Fig. 5 Time traces of axial velocity from four upstream probes ($P_2/P_{0R} = 0.9570 - 0.9577$, first mode P_0 perturbation).
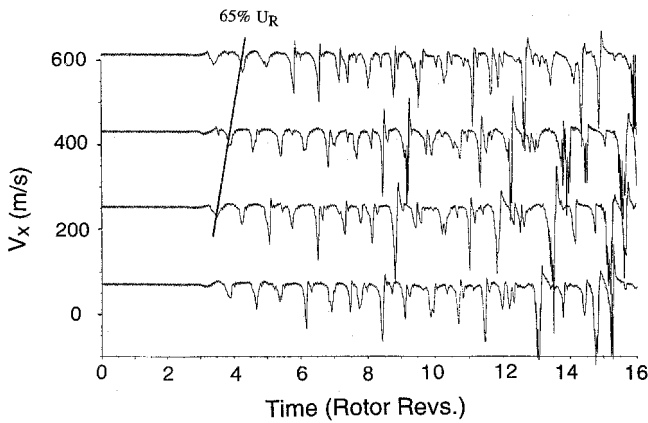
Fig. 6   Time traces of axial velocity from four upstream probes (P_2/P_{0R} = 0.9581 − 0.9589, second mode P_0 perturbation).
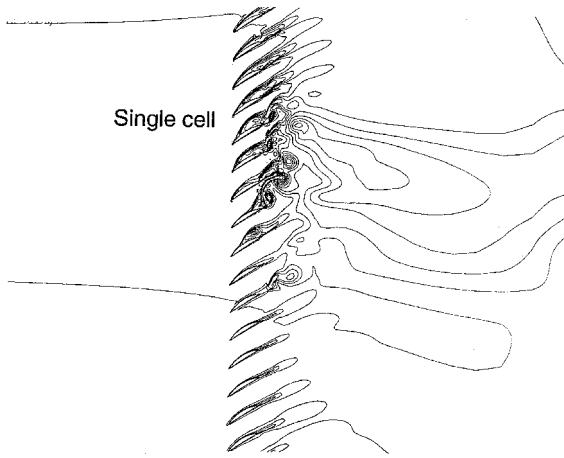

Fig. 7   Entropy contour showing a single-cell rotating-stall pattern under the first mode inlet stagnation pressure perturbation.

As far as the rotating speed of the stall cells is concerned, multiple cells clearly have higher absolute rotating speeds than a single cell. It might be more meaningful to interpret the results as that the shorter the stall cell scale, the higher the rotating speed. To understand the dependence of the cell speed on the length scale, it might be helpful to look at the situation in a rotor relative frame. For a blade passage, the time scale between the moment when the suction surface boundary layer is initiated to separate and the moment when the passage is fully stalled would depend largely on local development in terms of diffusion and convection of shear layers. This time scale could be considered independent of whether the rotating stall pattern had single or multiple cells. Consider an instant in time when a reference passage is fully stalled. The rotating speed of this stalled pattern would be effectively determined by how far the influence of this stalled passage could reach to cause a neighboring blade boundary layer to start to separate. The further the influence of the fully stalled passage could reach, the higher the relative rotating speed of the pattern would be. From this point of view, a stalled pattern with a longer spatial length scale would have a higher relative rotating speed.

Numerical tests were also carried out at shorter inlet/outlet duct lengths. It was found that if the inlet/outlet length was much shorter than the circumference, the short-scale rotating-stall patterns were always produced, whereas the long-scale single-cell pattern could not be generated even when the first mode of P_0 disturbance was applied at the inlet. It seems that to allow the long-scale first circumferential unstable mode to grow, the inlet/outlet duct length needs to be at least that similar to the circumference.

Table 1   Calculated parameters at stall inception (single blade row)

Inlet condition	Flow coefficient at stall inception	Number of cells	Cell rotating speed (in absolute frame)
Clean inlet	ϕ = 0.763	5–7	75–80% U_R
Second mode perturbation (Amp_0 = 0.003)	ϕ = 0.788	2	64–70% U_R
First mode perturbation (Amp_0 = 0.003)	ϕ = 0.810	1	53–58% U_R

Table 2   Calculated parameters at stall inception (two blade rows)

Blade numbers	Number of cells	Cell rotating speed (in absolute frame)
Ten rotor passages and nine stator passages	1	50% U_R
Ten rotor passages and 12 stator passages	2 (initial) 1 (final)	60% U_R (initial) 48% U_R (final)

B.   Two-Blade-Row (Rotor–Stator) Calculation

On the basis of the previous single-blade-row results, it is clear that external disturbances in the form of inlet stagnation pressure distortion can be influential in setting up a rotating-stall pattern. This suggests that the effect of blade-row interactions, inherent in turbomachines, should be examined. Here, a compressor stage with a rotor-row followed by a stator-row at a clean inlet (a uniform P_0) condition is considered. The rotor blades are the same as those used in the single-blade-row calculations with an absolute inflow angle of 0 deg and a rotating speed of 125 m/s. A double circular arc profile with 7% relative thickness is used for the stator blades. The stator blades are staggered to have a negative incidence to make sure that the rotor blade row would go into stall first when loaded by increasing the exit static pressure. The axial gap between the two blade rows is 40% chord length. Two cases were calculated with the parameters and the results summarized in Table 2.

For the rotor blade row, 10 blade passages are used. The number of blade passages for the stator row is chosen to produce a perturbation with a spatial length scale corresponding to the first or the second circumferential mode. A computational mesh for the case with 10 rotor passages and 12 stator passages is shown in Fig. 8.

The first calculation was for nine stator blade passages. The difference in the blade counts of the rotor and stator results in the two blade rows beating each other once per rotor revolution. Therefore, we should have a perturbation of the first mode caused by the blade-row interaction (i.e., the wavelength equals the circumference), as shown by a static pressure contour (Fig. 9) at an instant well before stall inception. Again, the four axial velocity probes were placed at a location 25% chord upstream of the rotor blade leading edge. The time traces during rotating stall inception when the exit static pressure was increased from P_2/P_0 = 1.0355 to 1.0370 are shown in Fig. 10. The plot clearly indicates a single-cell rotating-stall pattern, which is also shown by an instantaneous entropy contour in Fig. 11. Notice that in this case, a prestall wave pattern is quite visible from the time traces (Fig. 10).

A calculation was then performed with 10 rotor passages and 12 stator passages. This difference in rotor/stator blade numbers results in the second mode circumferential disturbance (i.e., a spatially periodic nonuniformity with its length-scale equal to half of the circumference). This spatially periodic disturbance is indicated by the instantaneous static pressure contours downstream of the stator blade row at a stable operating condition, as shown in Fig. 12. The time histories recorded from the four axial velocity probes are shown in Fig.
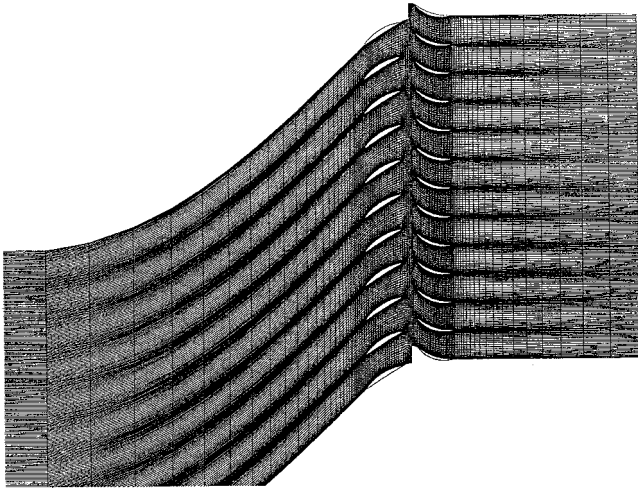
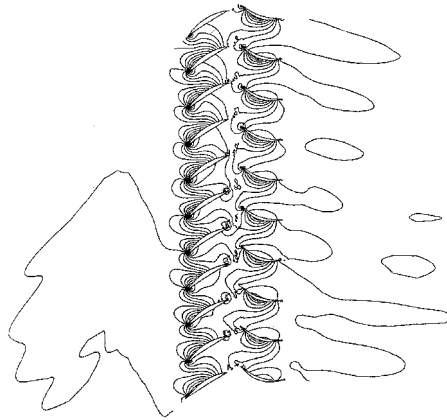Fig. 8   Computational mesh (NB_r = 10; NB_s = 12).

Fig. 9   Instantaneous static pressure contour at a stable flow condition (axial gap of 40% C; NB_r = 10; NB_s = 9).
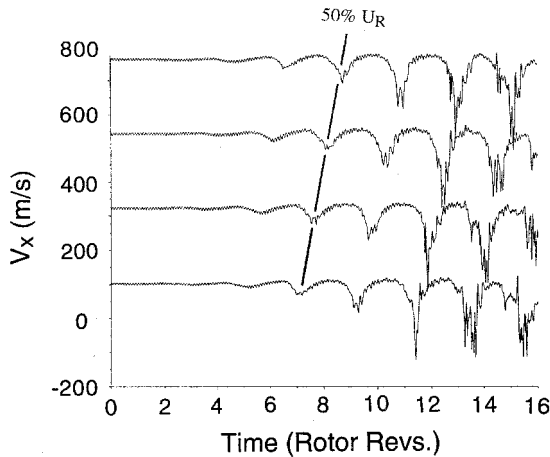

Fig. 10   Time traces of axial velocity from four upstream probes (axial gap of 40% C; P_2/P_0 = 1.0355 − 1.0370; NB_r = 10; NB_s = 9).

13. Note that for this case, a two-cell pattern is initiated by the second mode perturbation, as also shown in the instantaneous entropy contours (Fig. 14). However, at a higher loading condition, the two cells merged into a single cell. The change of pattern was first indicated by oscillatory developments of the two cells. Subsequently, one of the cells grew into a large single-cell and the other disappeared. Associated with this change of pattern, the rotating speed was observed to change
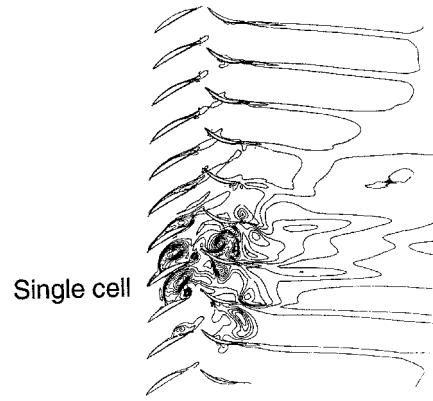

Fig. 11   Instantaneous entropy contour after stall inception (axial gap of 40% C; NB_r = 10; NB_s = 9).
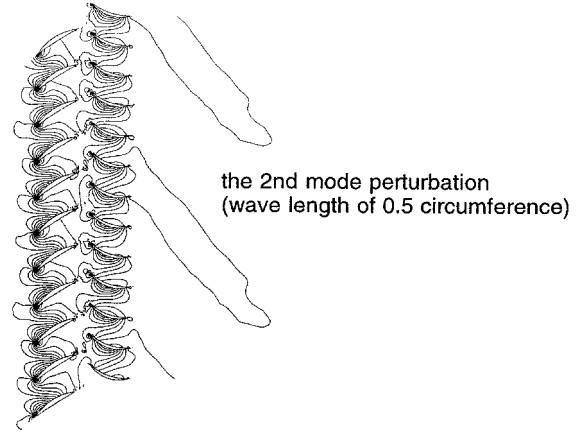

Fig. 12   Instantaneous static pressure contour at a stable flow condition (axial gap of 40% C; NB_r = 10; NB_s = 12).
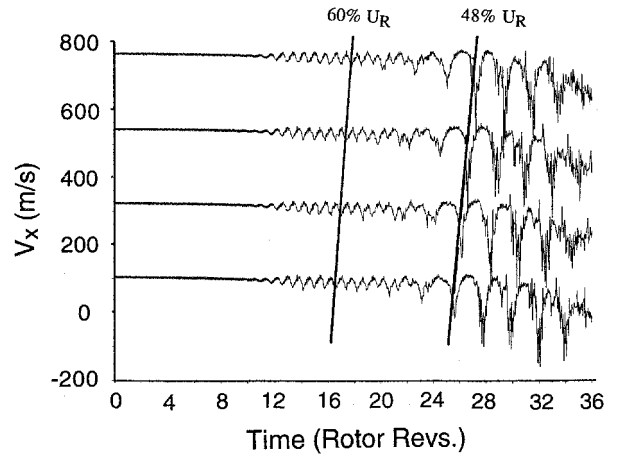

Fig. 13   Time traces of axial velocity from four upstream probes (axial gap of 40% C; P_2/P_0 = 1.0345 − 1.0380; NB_r = 10; NB_s = 12).

as well: the two initial cells rotated at an absolute speed of 60% U_R, whereas the final single cell rotated at about 48% U_R.

For both cases, the calculated single-cell rotating speed compares well with those observed in several experiments by Longley et al.[6]

C.   Discussion

Both the single-blade-row and multiple-blade-row results demonstrate that stall inception is sensitive to external disturbances. A multiple-cell pattern with a short-length-scale can be excited by a higher mode circumferential disturbance, al-
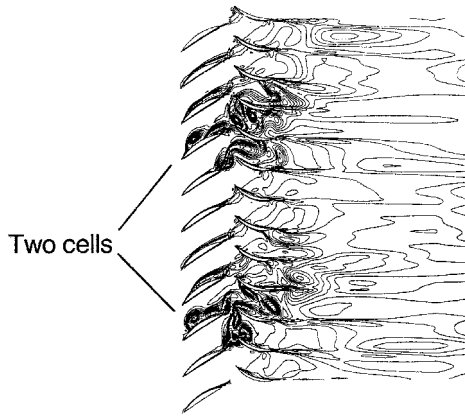
Fig. 14 Instantaneous entropy contour at initial stage of stall inception (axial gap of 40% C; NB_r = 10; NB_s = 12).

though a single-cell pattern is the most unstable one and, therefore, is most likely to come into being during stall inception.

As far as the rotor blade row is concerned, the temporal length scale of the perturbation resulting from the rotor–stator interaction is quite different from that caused from the stationary inlet stagnation pressure distortion in the single-row case. For the blade-row interaction, the time scale seen by a rotor blade is given by the stator blade passing frequency, whereas in the single-row case the time scale is given by the rotor revolution. In spite of the difference in the temporal length scale by a factor of 10 or so, the results for both cases seem to be consistent, indicating that the spatial length scale, instead of the temporal length scale, is the most relevant.

Comparison of all the calculated results reveals a general trend showing that a short-scale multicell pattern has more difficulty surviving and developing into a dominant rotating pattern in a two-blade-row situation than in a single-blade-row situation. In the single-blade-row calculations, a short-scale structure with a high rotating speed, once generated, would persist as the exit pressure was being further increased. While in a two-blade-row situation, all calculated results show that the initial stall structure would soon evolve into a long-scale single-cell rotating at a speed close to 50% blade rotation speed, even if it was initiated with a short-scale multicell pattern rotating at a higher speed.

The previously mentioned difference between single- and two-blade-row situations is highlighted by an additional calculated case. In this case, the rotor blade row with 10 blade passages was the same as in the previous two cases. The stator row had eight blade passages, so that the rotor–stator interaction resulted in a perturbation of the second-order circumferential mode. The axial gap between the two rows was narrowed to 20% chord. With this enhanced interaction of the second mode, one would expect a more persistent two-cell pattern. However, it turns out not to be the case. The time traces of axial velocity from the four upstream probes are shown in Fig. 15. It can be seen that a short-scale two-cell pattern becomes only just visible before being merged into the development of a single-cell pattern. Two different patterns are clearly indicated by their rotating speed: 63% U_R for the short-scale two-cell pattern and 48% U_R for the single long-scale single-cell pattern. As discussed earlier, during a transition from a two-cell pattern to a single-cell pattern, the two cells would develop in an oscillatory manner, which was manifested by one of the two cells being more visible than the other in a certain period of time.

Note that the scenario illustrated in Fig. 15 looks somehow similar to that observed in some experiments in which a short-scale spike appeared first rotating at high absolute speed (~70% U_R) for about one or two rotor revolutions before a long-scale single-cell pattern rotating at 40–50% U_R was formed.[5] In view of the present calculated results, it could be
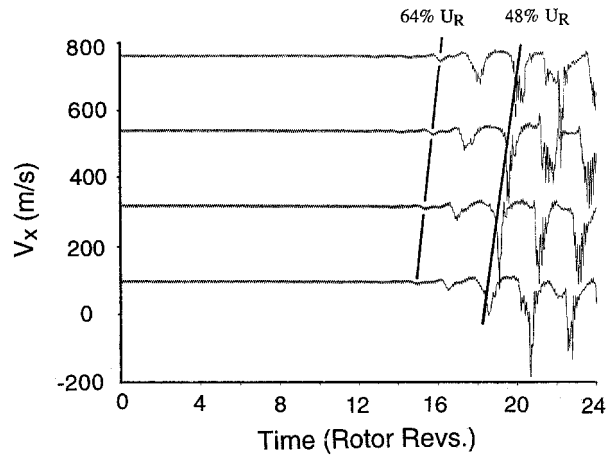

Fig. 15 Time traces of axial velocity from four upstream probes (axial gap of 20% C; P_2/P_0 = 1.0490 − 1.0505; NB_r = 10; NB_s = 8).

suspected that a short-scale single-cell spike might simply be one of multiple cells in the oscillatory developments, which was more developed than other cells before the multiple-cell pattern changed into a single-cell pattern.

In most rotating stall experiments in which a single-cell pattern was observed, test rigs with two or more blade rows were used. To the author's knowledge, one exception to this was a case in which a persistent and well-developed multiple-(three-) stall cell structure was observed.[8] In this case, the rotor row was not followed by a stator row and the inlet guide vane row was placed 4.5 chords upstream of the rotor row. As a result, the effect caused by the stator–rotor interaction was likely to be negligible. Hence, this experiment could be effectively regarded as a test with an isolated rotor blade row. Therefore, there seemed a greater likelihood that persistent short-scale multiple-cell patterns could exist in an isolated blade row.

Consider a cell rotating in the relative frame. In a two-blade-row situation, a short-scale pattern would rotate in the rotor frame at a slow relative speed (20–30% U_R), which means that the same pattern would have to rotate at a high speed (70–80% U_R) relative to the stator. This is apparently more difficult if the relative rotating speed of a stall pattern is closely associated with its spatial length scale, as argued earlier. On the other hand, if both blade rows have similar relative velocity triangles, a long-scale single-cell rotating at about 50% blade rotating speed seems to be the most likely pattern to suit a rotating stall development in both the rotor and stator rows. Therefore, there would be a tendency toward a single-cell pattern rotating at the speed compatible with both rotor and stator rows. Of course, the exact value of the compromised rotating speed might vary, depending on individual blade row geometry and flow conditions at stall.

IV.   Concluding Remarks

A numerical method with a quasi-three-dimensional time-marching Navier–Stokes solver has been developed for calculating rotating stall inception in axial flow compressors. The following points can be made based on the present computations.

1) Rotating stall pattern during its inception is sensitive to external disturbances in a form of a rotational or stationary circumferential nonuniformity. The initial onset pattern of rotating stall corresponds exactly to the spatial length scale of the circumferential nonuniformities. The first-order mode with the length-scale of the whole circumference is the least stable.

2) There is a close link between the rotating speed of a stall cell and its spatial length scale. The shorter the length scale, the higher the rotating speed in the absolute frame. A long-

scale single cell would rotate at about 50% blade speed. While a two-cell pattern with a shorter length scale has an absolute rotating speed of about 65% blade speed.

3) It is shown that a short-scale pattern is more difficult to survive in a multiple-blade-row situation than in an isolated blade-row situation. This might be because of the conflicting requirement that a short-scale pattern would have to travel in a rotor frame and a stator frame at two very different relative rotating speeds. In a two-blade-row situation, a transition from an excited short-scale two-cell pattern into a long-scale single-cell pattern is shown to be very likely. A hypothesis is proposed to establish a possible link between the pattern transition and the short-scale spike behavior as observed in some experiments.

Finally, it should be commented that there are many modeling aspects that need to be improved in the future. The main limitation of the present work is the two-dimensional model. The modeling of three-dimensional effects is expected to be important in resolving the issue of the short-scale spike mechanism during stall inception.

Acknowledgments

References

[1]Epstein, A. H., Ffowcs-Williams, J. E., and Greitzer, E. M., "Active Supersession of Aerodynamic Instabilities in Turbomachines," *Journal of Propulsion and Power*, Vol. 5, No. 2, 1989, pp. 204–211.

[2]Day, I. J., "Active Suppression of Rotating Stall and Surge in Axial Compressors," *Journal of Turbomachinery*, Vol. 115, No. 1, 1993, pp. 40–47.

[3]Moore, F. K., "A Theory of Rotating Stall of Multistage Compressors," *Journal of Engineering for Gas Turbines and Power*, Vol. 106, 1984, pp. 313–336.

[4]Moore, F. K., and Greitzer, E. M., "A Theory of Post-Stall Transients in Axial Compression Systems," *Journal of Engineering for Gas Turbines and Power*, Vol. 108, 1986, pp. 231–239.

[5]Day, I. J., "Stall Inception in Axial Flow Compressors," *Journal of Turbomachinery*, Vol. 115, No. 1, 1993, pp. 1–9.

[6]Longley, J. P., Shin, H.-W., Plumley, R. E., Silkowski, P. D., Day, I. J., Greitzer, E. M., Tan, C. S., and Wisler, D. C., "Effects of Rotating Inlet Distortion on Multistage Compressor Stability," *Journal of Turbomachinery*, Vol. 118, No. 2, 1996, pp. 181–188.

[7]Sisto, F., Wu, W., Thangam, S., and Jonnavithula, S., "Computational Aerodynamics of Oscillating Cascade with Evolution of Rotating Stall," *AIAA Journal*, Vol. 27, No. 4, 1989, pp. 462–471.

[8]Jonnavithula, S., Thangam, S., and Sisto, F., "Computational and Experimental Study of Stall Propagation in Axial Compressors," *AIAA Journal*, Vol. 28, No. 11, 1990, pp. 1945–1952.

[9]He, L., "New Two-Grid Acceleration Method for Unsteady Navier–Stokes Calculations," *Journal of Power and Propulsion*, Vol. 9, No. 2, 1993, pp. 272–280.

[10]He, L., "Integration of 2-D Fluid-Structure Coupled System for Calculations of Turbomachinery Aerodynamic/Aeroelastic Instabilities," *International Journal of Computational Fluid Dynamics*, Vol. 3, No. 4, 1994, pp. 217–231.

[11]Jameson, A., Schmidt, W., and Turkel, E., "Numerical Solutions of the Euler Equations by Finite Volume Method Using Runge-Kutta Time-Stepping Scheme," AIAA Paper 81-1259, 1981.

[12]Giles, M. B., "Non-Reflecting Boundary Conditions for Euler Equation Calculations," *AIAA Journal*, Vol. 28, No. 12, 1990, pp. 2050–2058.